# Lawrence Berkeley National Laboratory

**Title**
A Fluorination Method for Improving Cation-Disordered Rocksalt Cathode Performance

**Authors**
Ahn, Juhyeon
Chen, Dongchang
Chen, Guoying

Peer reviewed

# A Fluorination Method for Improving Cation-Disordered Rocksalt Cathode Performance

*Juhyeon Ahn, [a] Dongchang Chen [a] and Guoying Chen [a,*]*

[a.] *Energy Storage and Distributed Resources Division, Lawrence Berkeley National Laboratory, Berkeley, California 94720, USA*

[*] *Corresponding author's email: gchen@lbl.gov*

## Abstract

In Li-rich cation-disordered rocksalt oxide cathodes (DRX), partial fluorine (F) substitution in the oxygen anion sublattice can increase the capacity contribution from transition-metal (TM) redox while reducing that from the less reversible O redox. To date, limited fluorination substitution is achieved by introducing LiF precursor during the solid-state synthesis. To take full advantage of the fluorination effect, however, a higher F content is desired. In the present study, we report the successful use of a fluorinated polymeric precursor to increase the F solubility in DRX and the incorporation of F content up to 10-12.5 at. % into the rocksalt lattice of a model Li-Mn-Nb-O (LMNO) system, largely exceeding the 7.5 at. % limit achieved with LiF synthesis. Higher F content in the fluorinated-DRX (F-DRX) significantly improves electrochemical performance, with a reversible discharge capacity of ~ 255 mAh/g achieved at 10 at. % of F substitution. After 30 cycles, up to 40% increase in capacity retention is achieved through the fluorination. The study demonstrates the feasibility of using a new and effective fluorination process to synthesize advanced DRX cathode materials.

**TOC Graphic**
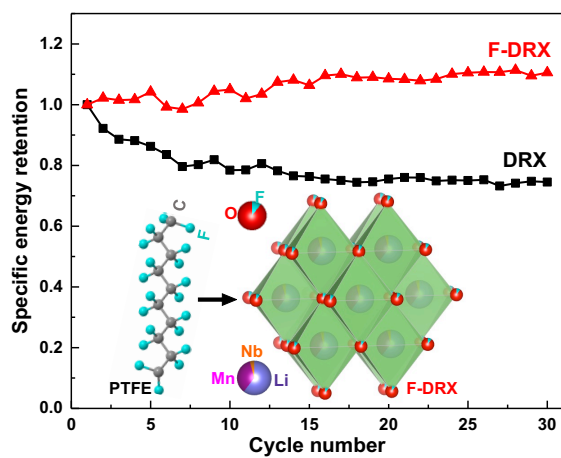
# 1. Introduction

With the growing demand for large-scale energy storage such as electric vehicles (EVs) and other energy storage systems (ESS), lithium-ion batteries (LIBs) are expected to meet the requirements on high energy and power densities, low cost and long life, all of which are predominately determined by the intrinsic characteristics of the electrode materials.[1–3] In recent years, lithium-rich cation-disordered rocksalt oxide cathodes have received significant attention because of their Co-free chemistry, high energy density (> 1,000 Wh/kg) and high operating voltages,[4,5] making them attractive alternatives to the conventional layered cathode materials such as lithium nickel manganese cobalt oxides ($LiNi_xMn_yCo_{1-x-y}O_2$, NMCs).[6,7] The large charge storage capacity in the DRX materials is attributed to the collective redox activities from a single- or multi-electron pairs of TM cations, such as $Ni^{2+}/Ni^{3+}$,[8] $Ni^{2+}/Ni^{4+}$,[9–11] $Mn^{2+}/Mn^{4+}$,[12–14] $Mn^{3+}/Mn^{4+}$,[9,13,15–17] $V^{3+}/V^{4+}$,[18,19] $V^{4+}/V^{5+}$,[14] $Cr^{3+}/Cr^{6+}$,[19] $Mo^{3+}/Mo^{5+}$,[20] and $Mo^{3+}/Mo^{6+}$,[21] and oxygen anions ($O^{2-}/O^{n-}$, $0 \leq n < 2$).[22-25] On the other hand, the $d^0$ TM elements (*e.g*, $4d$ $Ti^{4+}$ and $Cr^{6+}$ as well as $5d$ $Nb^{5+}$ and $Mo^{6+}$) are essential for structural stability but they remain electrochemically inactive.[5,26]

The reversibility of the oxygen anionic redox activity is believed to be much poorer compared to that of the cation redox when operates at high upper voltage, impeding the overall long-term cycling stability of these newer cathode materials.[27] In developing mitigation approaches to the drawback of irreversible oxygen redox behavior, computational modeling and experimental studies on partial substitution of oxygen by fluorine was attemped.[8–21,28] Table S1 lists the fluorinated-DRX compounds reported in the literature so far. In general, the F-DRX cathodes were found to have better performance compared to their oxide counterparts, with less oxygen release, less impedance rise and better cycling stability.[8,15,20]

The substitution of oxygen by fluorine is traditionally achieved by introducing LiF precursor during F-DRX synthesis. As F and Li share stronger bonding than that between F and TM, the lack in thermodynamic driving force limits the overall solubility of LiF in DRX.[28] Several factors such as chemical composition (Li content, oxidation state of the redox-active TM and $d^0$ TM), precursor choices, synthesis method (solid-state, solvothermal and ball-milling etc.), synthesis temperature and duration were found to influence F solubility.[8–21] For example, higher levels of F substitution were recently achieved on DRX compounds such as $Li_{(1.333)}$-$Mn^{3+}$-$Mn^{4+}$-O-F,[13] $Li_2(Mn^{2+})_2Nb_{1/3}O_2F$ and $Li_2(Mn^{2+})_{1/2}Ti_{1/2}O_2F$.[12] These samples were synthesized through a prolonged high-energy ball-milling route rather than the typical solid-state process, making them difficult for commercial scale-up. For a given composition space such as the $Li_{(1.2)}$-$Mn^{3+}$-$Nb^{5+}$-O-F (LMNOF) system using the solid-state synthesis method, it was found that significant LiF phase segregation occurs upon increasing the F content to beyond ~ 7.5 at. %.[15] This largely limits the ability in utilizing F substitution to improve the performance of DRX cathode materials.

In this study, we explore the possibility of using an alternative F source for DRX fluorination based on the LMNO model system. A fluorinated polymeric precursor, poly(tetrafluoroethylene) (PTFE) with a chemical formula of $(CF_2–CF_2)_n$, was selected as a F precursor during the solid-state synthesis. A series of F-DRX with the chemical formula of $Li_{1.2}Mn_{0.6+0.5x}Nb_{0.2-0.5x}O_{2-x}F_x$ (LMNOF, $0 < x \leq 0.4$) were synthesized. For the first time, we show that higher F solubility, at least 10 at. %, can be achieved in $Nb^{5+}$-containing and $Mn^{3+}$-redox active DRX, exceeding the observed F solubility limit when LiF was used as F precursor. The addition of the small amount of carbon upon PTFE decomposition boosts DRX conductivity and further improves electrochemical performance. We compare the crystallinity, chemistry and electronic structures of the LMNOF series by using X-ray diffraction (XRD), hard and soft X-ray

absorption spectroscopy (hXAS and sXAS), inductively coupled plasma (ICP) spectroscopy and F ion selective electrode (F-ISE) analysis. The homogeneity of the samples and elemental distribution at the particle-level were evaluated by using scanning electron microscopy (SEM) and energy-dispersive X-ray (EDX) mapping. The reversibility of cationic and anionic redox behavior as a function of fluorination degree in the F-DRX materials is also discussed.

## 2. Results and Discussion

### 2.1 Synthesis and characterization of LMNOF

In solid-state synthesis reactions, careful control in annealing temperature is critical in order to produce phase-pure crystalline DRX materials. The synthesis of LMNO based DRX often requires a high annealing temperature of more than 950 °C.[29,30] PTFE was previously used as F source to incorporate F anions into TM oxide lattices. For example, the successful fluorination of monoclinic-structured $Nb_2O_5$ by PTFE was achieved at 950 °C, enabled by the favorable presence of Nb–F environment.[31] Here, the optimal temperature that allows for simultaneously degradation of PTFE and the formation of the phase-pure cation-disordering structure was investigated. A series of DRX materials with varying level of F content, including $Li_{1.2}Mn_{0.6}Nb_{0.2}O_2$ (F0), $Li_{1.2}Mn_{0.625}Nb_{0.175}O_{1.95}F_{0.05}$ (F2.5), $Li_{1.2}Mn_{0.65}Nb_{0.15}O_{1.9}F_{0.1}$ (F5), $Li_{1.2}Mn_{0.7}Nb_{0.1}O_{1.8}F_{0.2}$ (F10), $Li_{1.2}Mn_{0.725}Nb_{0.75}O_{1.75}F_{0.25}$ (F12.5), $Li_{1.2}Mn_{0.75}Nb_{0.05}O_{1.7}F_{0.3}$ (F15) and $Li_{1.2}Mn_{0.8}O_{1.6}F_{0.4}$ (F20) that correspond to an F content of 0, 2.5, 5, 10, 15 and 20 at. %, respectively, were prepared after experimenting with synthesis temperatures. For example, impurity phases were found during the synthesis of F2.5 at an annealing temperature of either 750 °C or 950 °C, although crystalline

PTFE and LiF were not detected in both cases (Fig. S1). Phase-pure F2.5 were obtained when the synthesis temperature was increased to 1,000 °C.

Fig. 1a shows the powder XRD patterns collected on pristine F0, F2.5, F5 and F10. All patterns were indexed to the cubic rocksalt crystal structure with a $Fm\bar{3}m$ space group, with no impurities detected. Fig. S2 shows the Rietveld refinements of the XRD patterns. The combined results confirm a continuous decrease in lattice parameter with the increase in F content, ranging from 4.1866 Å for F0, 4.1863 Å for F2.5, 4.1794 Å for F5 and 4.1773 Å for F10, respectively. Further increase in F content to 12.5 at. % leads to the formation of a small amount of impurity phases, including LiF, as shown Fig. S3. This suggests that F solubility between 10-12.5 at. % can be achieved when PTFE is used as the F precursor, largely exceeding what was observed when LiF was used as F precursor. In the latter case, the formation of LiF secondary phase is significant beyond the 7.5 at. % limit.[15] The presence of impurity phases greatly enhanced when further increase F content to beyond 12.5 at. %, with the cubic rocksalt structure no longer obtained on the F20 sample with 20 at. % of F. This is likely a result of low Nb content in the compounds, as it is known that $d^0$ TM ($Nb^{5+}$ in this case) plays a critical role in the formation of cation-disordered rocksalt crystal structure.[5,32] The increase of F solubility with PTFE is likely a result of changes in competing phases present during the synthesis. Thermodynamically, precursors with higher F chemical potential is less stable and therefore provides a larger driving force for high F solubility in DRX. LiF is one of the most stable F containing phases that has a melting point of 848.2 °C. PTFE, on the other hand, melts at a much lower temperature of 327 °C and decomposes before 500 °C.[33] This renders PTFE a more superior fluorination precursor than LiF.

The particle morphology and elemental distribution of the as-prepared F-DRX samples were further examined by using SEM and EDX mapping, respectively. The average primary

particle size of F0 is ~ 10 μm, with the majority of the particles adopting irregular shapes (Fig. 1b–e). Fluorine substitution generally increases the particle size. As shown in Fig. 1b, the average particle size of F2.5 increased to ~ 20–30 μm. As the F content increases, the particle size further increases, with the average size reaching ~ 30–50 μm for F5 and F10, respectively. Uniform elemental distribution of Mn, Nb, O and F at both bulk- and particle-levels is observed on all samples, as shown in Fig. 1b–e and Fig. S4, respectively. The elemental composition determined from EDX spectroscopy are shown in Fig. S5 and summarized in Table S2. The ratio between Mn and Nb is consistent with the theoretical values as well as those determined by ICP measurements (Table S3). Accurately quantifying the F content in the F-DRX is challenging as most analytical techniques cannot differentiate the presence of F in the rocksalt lattice *vs*. impurities such as LiF. Solid-state NMR is one of those few exceptions where a combination of $^7$Li and $^{19}$F NMR analysis can distinguish the incorporation of bulk F in the DRX structure from F-containing diamagnetic impurities or domains. However, due to the broad nature of the chemical shift distribution, quantification of F content within the F-DRX series remains difficult. Here an alternative method of using fluoride ion selective electrode was adopted to determine the F content in the series. Although the technique measures the total amount of F present in the bulk sample, in the absence of impurities, the level of F substitution in DRX can be determined and the results are listed in Table S3. The measured F contents are consistent with the targeted value in each sample, confirming the high quality of the synthesized F-DRX samples.

Hard and soft X-ray absorption spectroscopy were used to investigate the bulk and surface chemistry of the samples. Fig. 2a shows the X-ray absorption near-edge structure (XANES) spectroscopy of Mn *K*-edge collected on the pristine F0, F2.5, F5 and F10. The energy position at the first derivative of the rising-edge is often used to index the oxidation state of TMs.[34] A shift

towards higher energy corresponds to an increase in TM oxidation state while lower energy shift indicates TM reduction. The $K$-edge energy positions for F0, F2.5, F5 and F10 are nearly constant at ~ 6548 eV, consistent with the energy position of $Mn_2O_3$ (Mn(III)), as shown in the standard spectra of Mn at various oxidation states (Fig. S6). This suggests that bulk Mn remains at the trivalent state in all pristine DRX samples. Mn $L$-edge sXAS spectra were also collected using both total electron yield (TEY) and total fluorescence yield (FY) detectors, and the results on the same set of samples are shown in Fig. 2b. While the TEY profiles (thick line) represent signals from the top surface layer of ~ 5 nm, the FY signals (shown in thin lines) arise from the deeper subsurface region of ~ 50 nm.[35] The broad $L_3$-edge absorption near 640.8 eV is a clear indication of Mn(III) features, as both peak position and profile match well with that of $Mn_2O_3$ standard (shown in the black line).[26,36] For comparison purpose, the reference spectra collected on MnO (II), $Mn_2O_3$ (III) and $MnO_2$ (IV) are also shown in Fig. S7. The observation of $Mn^{3+}$ cations both in the bulk and on the surface in all three F-DRX provides further evidence on the successful incorporation of F into the rocksalt lattice. We note that the decomposition of PTFE also introduces a small amount of carbon which often reduces $Mn^{3+}$ to $Mn^{2+}$ during the synthesis. Although $Mn^{2+}$ presence was not observed in F2.5, F5 and F10, in the case of F15 and F20 where a higher amount of PTFE was used for synthesis, $Mn^{2+}$ was found by the soft XAS measurements.

Fig. 2c and 2d show the normalized sXAS spectra for the Nb $M_{4,5}$-edge and O $K$-edge, respectively. The presence of $Nb^{5+}$ cation is evidenced by the Nb $M$-edge peaks through the low energy scan where changes were not observed upon the incorporation of F anions. It is known that the pre-edge peak below 533 eV on the O $K$-edge spectrum corresponds to the unoccupied $2p$ states in the hybridization of TM-$3d$ and O-$2p$.[37] The O pre-edge peaks for F0 and F2.5 are nearly identical, indicating that at low F content, the effect on oxygen electronic structure is minimal. On

the other hand, with F content over 5 at. %, the intensity of the shoulder peak at ~ 533 eV increases significantly, leading to the splitting peak feature centered at about 531 eV. This suggests that the presence of a larger amount of F disrupts O electronic structure in the rocksalt lattice. As the broad band above 533 eV corresponds to the hybridized states of TM-*4sp* and O-*2p* orbitals relating to the metal-ligand bond distance,[38] the shift towards higher energy in F10 signifies the shortening of metal-oxygen bonding distance in the sample. Further investigation on the F *K*-edge spectra (Fig. 2e and 2f) confirms the presence of F species in all F-DRX, although it is unclear whether F resides in the rocksalt lattice or appears on an impurity phase, commonly LiF. Upon comparison with the standard spectrum of LiF which exhibits strong peaks at 691 and 700 eV as well as a broad band between 707 and 730 eV (Fig. 2e),[39,40] it can be seen that the TEY and FY F signals detected on F2.5, F5 and F10 are different from those of LiF, further confirming the incorporation of F in the DRX lattice both in the subsurface region as well as on the surface. On the other hand, distinct LiF-like features are observed in both TEY and FY spectra collected on F15 and F20 samples with higher F contents (Fig. 2f). We found that the formation of LiF is also promoted by lower synthesis temperature. For example, LiF formation were detected when synthesis of F2.5 was carried out at 750 °C, as shown by both TEY and FY modes. The signal, however, disappears upon increasing the annealing temperature to 950 °C (Fig. S8).

*2.2. Electrochemical Performance of LMNOF cathodes*

To evaluate the electrochemistry, the DRX active materials were first ball-milled with a carbon additive in a weight ratio of 8:2. The process effectively breaks down the large DRX particles to a similar average particle size of ~ 1 μm for all samples (Fig. S9). In fabricating the

composite cathodes, the prepared mixture was then blended with a carbon additive and a PVDF binder in a weight ratio of 7:2:1. The fraction of the active mass loading in the electrode is therefore 56 wt.%. Fig. 3 compares half-cell electrochemical performance of the non-fluorinated (F0) and fluorinated (F2.5, F5 and F10) DRX cathodes when cycled between 1.5–4.8 V at a current rate of 10 mA/g. The theoretical capacities based on the total Li content (1.2 mole of Li per formula unit) are 350, 353, 356 and 363 mAh/g for F0, F2.5, F5 and F10, respectively, of which 175, 184, 193 and 212 mAh/g comes from the contribution of $Mn^{3+}/Mn^{4+}$ redox couple (Table 1). As shown in the charge and discharge voltage profiles and the corresponding differential capacity $vs$. voltage ($d$Q/$d$V) plots (Fig. 3a–d), the initial charge voltage curve of the non-fluorinated F0 displays a sloping region at low voltages and a distinct "flatter" region at high voltages, indexed as region $A$ and $B$, respectively (Fig. 3a). In the LMNO system, $Nb^{5+}$ cation is known to remain electrochemically inactive.[5,26] Using a combination of electrochemical characterization techniques, synchrotron X-ray diffraction, soft and hard X-ray absorption, resonant inelastic X-ray scattering and differential electrochemical mass spectroscopy, previous studies have primarily attributed region $A$ and $B$ to the cationic Mn redox and anionic O redox, respectively, with the latter involving the oxidation of $O^{2-}$ to $O^{n-}$ ($0 < n < 2$) and $O_2$ gas evolution.[15,26,30,41,42] The two regions are also indexed as $A'$ and $B'$ in the $d$Q/$d$V plot (Fig. 3b). Careful comparison shows that O redox activities in the $B'$ region tends to decrease with increasing F content in DRX, with the changes between F5 and F10 particularly significant. In the case of F10, the decrease in the O redox peak is in a remarkable contrast to the sharper and more intense Mn redox peak at region $A'$, confirming increasing fraction of capacity contribution from the Mn cationic redox. The overall capacity of the F-DRX materials decreases with the increase in F substitution, with an initial discharge capacity of ~ 269, 270, 241 and 207 mAh/g obtained on F0, F2.5, F5 and F10 cathodes,

respectively (Table 1). We note that the first cycle irreversible capacity loss (ICL) increases while the coulombic efficiency decreases with the increase in F content (Fig. 3a). In the second cycle, however, the ICL becomes lower in the F-DRX than that in the non-fluorinated DRX (Fig. 3c). In all samples, the potential for the first redox peak arising from Mn redox (*C'*, Fig. 3d) is lower than that in the first cycle. The O redox active region (*D*) is significantly reduced than that in the first cycle, which is shown by a lower intensity of the cathodic peak (*D'*) as well. These differences are likely related to the changes in cathode-electrolyte interfacial chemistry between DRX and F-DRX.[43,44] Detailed studies are currently underway, and the results will be reported in a following publication.

Fig. 3e summarizes the 1st, 2nd and 3rd cycle charge capacity contribution as a function of F content. Assuming the contribution from the $Mn^{3+}/Mn^{4+}$ redox couple remain constant in all three cycles, the capacity contribution from the O oxidation varies with F content as well as cycle number. With the increase in F content from 0 to 2.5, 5 and 10 at. %, O redox capacity contribution in the first cycle (grey bar) decreases from ~ 136 to 130, 100 and 59 mAh/g, respectively. These values correspond to 44%, 42%, 34% and 22% of the initial charge capacity. The O oxidation capacity contribution in the second cycle (blue bar) becomes much lower, with 101, 89, 51 and 12 mAh/g obtained on F0, F2.5, F5 and F10, respectively, corresponding to 37%, 33%, 21% and 5% of the charge capacities. While O capacity appears to stabilize after the second cycle in F-DRX, evidenced by the same contribution between the second and third cycle (magenta bar), the value in F0 continues to decrease (Fig. S10). After three cycles, the O contribution in F0 is reduced to 31%. The results suggest an overall lower O capacity contribution and more reversible nature of oxygen redox in the F-DRX materials.

Fig. 4a and 4b compare the cycling stability of the cathodes. While the initial capacity is lower in F-DRX, the capacity retention is much improved. After 30 cycles, the remaining discharge capacities were 226, 247, 226, 254 mAh/g for F0, F2.5, F5 and F10, respectively, corresponding to a capacity retention of 84%, 92%, 94% and 123%. The unusual increase in capacity along with cycling in F10 is likely a result of changes in Mn redox chemistry or enhanced contribution from O redox. Detailed computational, characterization and mechanistic studies are currently underway to understand the source of capacity increase. The average voltage is also an important metrics in characterizing the cycling stability of cathode materials with anionic redox activities.[42,45] Fig. S11a and S11b show the average voltage and the voltage retention during the first 30 cycles of the DRX cathodes. While voltage decay was broadly observed, voltage retention was much improved with fluorination. During the first 30 cycles, the average voltage decreased about 300 and 250 mV for F2.5 and F10, respectively, with the latter showing the best performance in the series. The results are consistent with the improved reversibility and stability of O redox in F-DRX.

Fig. S11c and S11d compare the specific discharge energy and energy retention upon the cycling of the cathodes. The initial energy densities of F0 and F2.5 were over 855 Wh/kg while that of F5 and F10 were about 770 and 640 Wh/kg, respectively. After 30 cycles, the energy densities in F0 and F5 were reduced to lower than 645 Wh/kg while those of F2.5 and F10 were at about 700 and 710 Wh/kg, respectively. This corresponds to about 82% and 84% of energy retention in F2.5 and F5, respectively, while the retention in F0 was 75%. F2.5 synthesized with LiF precursor also showed a similar lower retention of ~76%. On the other hand, the energy retention in F10 improves with cycling, clearly demonstrating superior cathode performance as it reaches about 110% increase after 30 cycles.

We further compared the performance of F-DRX samples made with PTFE and LiF precursors. Due to the limited F solubility previously described, only F2.5 and F5 in the series can be made phase-pure by using LiF as the F precursor. Fig. 4c-d and Fig. S12 show the electrochemical performance obtained on F2.5 cathode prepared from PTFE and LiF. In the 1st cycle charge/discharge voltage profile and the corresponding $dQ/dV$ plot (Fig. S12a and S12b), a slight reduction in polarization was observed in PTFE sample. After 30 cycles, the discharge capacity was 247 and 225 mAh/g for PTFE and LiF samples, respectively, corresponding to capacity retention of 92% and 85%. The same trend is also observed on the specific energy and energy retention, as shown in Fig. S12c and S12d. We believe the introduction of a small amount of carbon, resulting from the decomposition of the PTFE polymer, may play a role in the enhanced electrochemical performance. Previous studies have shown that a small amount of well-dispersed carbon additive can significantly improve the electronic conductivity of electrode materials, particularly in poor electronic conductors such as $LiFePO_4$.[46–48] Assuming no C loss during the heat treatment, the calculated added carbon content is 0.46, 0.92 and 1.88 wt. % for F2.5, F5 and F10, respectively.

Kinetic properties were evaluated by carrying out the rate capability analysis in the voltage window of 1.5-4.8 V. While the voltage profiles remain similar (Figure 5a-d), the discharge capacity decreases with the increase of current density in all DRX cathodes. As current densities increased from 10 to 200 mA/g, the discharge capacities decreased from 257, 260, 231 and 205 mAh/g to 122, 130, 114 and 100 mAh/g in F0, F2.5, F5 and F10, respectively (Fig. 5e and 5f). In general, the rate capability increases with fluorination, likely due to improvements in both ionic and electronic conductivities. A direct correlation to the level of fluorination, however, was not observed.

## 3. Conclusions

In summary, a novel synthesis approach was developed to incorporate fluorine anions into the disordered rocksalt crystal structure. By utilizing a fluoropolymer precursor, higher F content of 10-12.5 at. % was made possible in DRX materials. Increasing F content reduces the irreversible oxygen redox activities while increasing the cationic redox contribution to the capacity, leading to an overall more stable cathode material. Although the initial discharge capacity was slightly lower than that in the nonfluorinated DRX, F-DRX shows superior electrochemical stability over long term cycling. This study opens up a new route for chemical fluorination, enabling better use of combined TM and O redox activities in Li-rich TM oxide cathodes.

## 4. Experimental

*4.1 Synthesis*

To synthesize the F-DRX materials, stoichiometric amounts of $Li_2CO_3$($\geq$ 99.0%, ACS reagent), $Mn_2O_3$ (99.9%, ACS reagent), $Nb_2O_5$ (99%, ACS reagent), poly(tetrafluoroethylene) (PTFE, mean particle size of 6–9 microns, Goodfellow) and ethanol were mixed in a planetary ball mill (PM-100, Retsch) at the speed of 200 rpm for 18 hr. For $Li_{1.2}Mn_{0.6}Nb_{0.2}O_2$, the same precursors were used except PTFE. Typically, 10 mol. % extra $Li_2CO_3$ was used to compensate possible Li loss during calcination. After drying the mixture for 12 hr, the collected powder was gently grinded in a mortar and pestle and annealed at 1,000 °C for 12 hr under the flow of Argon gas (99.998 %, Praxair). The ramp rates for both heating and cooling were 5 °C/min. The as-synthesized powder was further grinded in the Argon filled glove box ($O_2$ < 1 ppm and $H_2O$ < 1

14

ppm) before storage. The synthesis of F2.5 using LiF followed the same procedure except LiF (99.98 %, Alfa Aesar) was used instead of PTFE.

*4.2 Characterization*

The chemical composition was determined by inductively coupled plasma optical emission spectrometers (PerkinElmer optima 5300 DV). Fluorine content was determined using a fluorine ion selective electrode (UX-27504-14) measurement. The powder samples were dissolved in the mixture of $HNO_3$ (70%) and HCl (36.5–38.0%, Sigma-Aldrich) and then diluted by using sodium acetate and fluoride ionic strength adjuster (TISAB, Cole-Parmer). The F concentration was calculated from the measured ISE potential at room temperature (~19 °C) using the calibration curve of $E_{cell} = K - 0.0569 \log [F^-]$, where $K = 0.11823$. The powder X-ray diffraction was analyzed by a Bruker D2 powder X-ray diffractometer (Cu Kα, 40 kV, 30 mA, λ = 1.54 Angstrom). The refinement of the XRD patterns was performed using a Fullprof software. The morphological images were taken by a Field Emission Scanning Electron Microscopy (JEOL 7500F) at 15 KV. Energy-dispersive X-ray spectroscopy and EDX mapping were collected at 8 kV by using the NSS configuration software. XANES spectra were collected using hard X-ray absorption spectroscopy at Stanford Synchrotron Radiation Lightsource (SSRL) beam line 2-2 and the data was processed using a Sam's Interface for XAS Package (SIXPACK) software. Electrode samples sandwiched between Kapton tapes were placed at 45° to the incident X-ray beam. Soft X-ray absorption spectroscopy analysis for the as-synthesized powder samples was conducted at SSRL beam line 10-1 and 8-2. Spectral measurements were performed on the 31-pole wiggler with a ring current of 350 mA, a 1000 line $mm^{-1}$ grating monochromator with 20 mm entrance and exit slits, and a 1 $mm^2$ beam spot. XAS profiles were collected under ultrahigh vacuum ($10^{-9}$ Torr). For the Mn(II),

Mn(III), and Mn(IV) standards, MnO, $Mn_2O_3$, and $MnO_2$ powders were used, respectively. The data was processed using the Pymca software.

*4.3 Electrochemical evaluation*

For electrode preparation, the active materials were ball-milled with a carbon (acetylene black) in 8:2 weigh ratio at a speed of 300 rpm for 12 hr. The obtained mixture was then blended with acetylene black (Denka) and polyvinylidene fluoride (PVDF) binder (Kynar flex 2801) that was dissolved in NMP in a weight ratio of 7:2:1. After thoroughly blended by using the Thinky mixer (AR-100, Thinky Inc.) for 15 min, the slurry was cast onto an aluminum current collector and then dried at 120 °C in a vacuum oven. The average active material loading was ~ 1.5 mg/cm$^2$. The 2032-type coin-cell half cells were assembled with 1M $LiPF_6$ in 1:1 (v/v) of ethylene carbonate (EC): diethylene carbonate (DEC) (Novolyte Technologies Inc.) electrolyte and a microporous trilayer membrane (PP/PE/PP, Celgard 2325) separator. Lithium foil (Alfa Aesar) was used as counter and reference electrodes. The electrochemical measurements were carried out with the constant current mode between 4.8 and 1.5 V at a current rate of 10 mA/g at room temperature using a VMP3 battery potentiostat (Bio-Logic science). The rate performance was evaluated between 4.8 and 1.5 V at a varying current density of 10, 20, 40, 100 and 200 mA/g. All charge and discharge capacities were calculated based on the net active material loading on the electrode.

**ASSOCIATED CONTENT**

**Supporting Information Available:** Additional data and figures including XRD patterns, XRD refinements, SEM images and EDX elemental mapping, elemental analysis, hard and soft XAS spectra and electrochemical performance are included.

## Author Information

Corresponding Author

*E-mail: gchen@lbl.gov

Coauthors

*E-mail: juahn@lbl.gov

*E-mail: dongchangchen@lbl.gov

## Notes

The authors declare no conflict of interest.

**References**

1. M. S. Whittingham, Lithium Batteries and Cathode Materials, *Chem. Rev.* 104, 2004, 4271–4302.

2. J. B. Goodenough, Y. Kim, Challenges for Rechargeable Li Batteries, *Chem. Mater.* 22, 2010, 587–603.

3. J.-M. Tarascon, M. Armand, Issues and Challenges Facing Rechargeable Lithium Batteries, *Nature* 414, 2001, 359–367.

4. J. Lee, A. Urban, X. Li, D. Su, G. Hautier, G. Ceder, Unlocking the Potential of Cation-Disordered Oxides for Rechargeable Lithium Batteries, *Science* 343, 2014. 519–522.

5. R. J. Clement, Z. Lun, G. Ceder, Cation-Disordered Rocksalt Transition Metal Oxides and Oxyfluorides for High Energy Lithium-Ion Cathodes, *Energy Environ. Sci.* 13, 2020, 345–373.

6. N. Nitta, F. Wu, J. T. Lee, G. Yushin, Li-Ion Battery Materials: Present and Future, *Mat. Today*, 18, 2015, 252–264.

7. J. Ahn, D. Susanto, J.-K. Noh, G. Ali, B. W. Cho, K. Y. Chung, J. H. Kim, S. H. Oh, Achieving High Capacity and Rate Capability in Layered Lithium Transition Metal Oxide Cathodes for Lithium-Ion Batteries, *J. Power Sources* 360, 2017, 575–584.

8. J. Lee, J. K. Papp, R. J. Clément, S. Sallis, D.-H. Kwon, T. Shi, W. Yang, B. D. McCloskey, G. Ceder, Mitigating Oxygen Loss to Improve the Cycling Performance of High Capacity Cation-Disordered Cathode Materials, *Nat. Commun.* 8, 2017, 981.

9. B. Ouyang, N. Artrith, Z. Lun, Z. Jadidi, D. A. Kitchaev, H. Ji, A. Urban, G. Ceder, Effect Fluorination on Lithium Transport and Short-Range Order in Disordered-Rocksalt-Type Lithium-Ion Battery Cathodes, *Adv. Energy Mater.* 2020, 1903240.

10. E. Zhao, L. He, B. Wang, X. Li, J. Zhang, Y. Wu, J. Chen, S. Zhang, T. Liang, Y. Chen, X. Yu, H. Li, L. Chen, X. Huang, H. Chen, F. Wang, Structural and Mechanistic Revelations on High Capacity Cation-Disordered Li-Rich Oxides for Rechargeable Li-Ion Batteries, *Energy Storage Mater.* 16, 2019, 354–363.

11. H. Ji, D. A. Kitchaev, Z. Lun, H. Kim, E. Foley, D.-H. Kwon, Y. Tian, M. Balasubramanian, M. Bianchini, Z. Cai, R. J. Clément, J. C. Kim and G. Ceder, Computational Investigation and Experimental Realization of Disordered High-Capacity Li-Ion Cathodes Based on Ni Redox, *Chem. Mater.* 31, 2019, 2431–2442.

12. J. Lee, D. A. Kitchaev, D.-H. Kwon, C.-W. Lee, J. K. Papp, Y.-S. Liu, Z. Lun, R. J. Clément, T. Shi, B. D. McCloskey, J. Guo, M. Balasubramanian, G. Ceder, Reversible $Mn^{2+}/Mn^{4+}$ Double Redox in Lithium-Excess Cathode Materials. *Nature* 556, 2018, 185–190.

13. Z. Lun, B. Ouyang, H. Kim, Z. Cai, R. J. Clement, D.-H. Kwon, J. Huang, J. K. Papp, M. Balasubramanian, Y. Tian, B. D. McCloskey, H. Ji, H. Kim, D. Kitchaev, G. Ceder, Design Principles for High-Capacity Mn-Based Cation-Disordered Rocksalt Cathodes, *Chem* 6, 2020, 153–168.

14. D. A. Kitchaev, Z. Lun, W. D. Richards, H. Ji, R. J. Clément, M. Balasubramanian, D.-H. Kwon, K. Dai, J. K. Papp, T. Lei, B. D. McCloskey, W. Yang, J. Lee, G. Ceder, Design Principles for High Transition Metal Capacity in Disordered Rocksalt Li-Ion Cathodes, *Energy Environ. Sci.* 104, 2018, 2159–2171.

15. Z. Lun, B. Ouyang, D. A. Kitchaev, R. J. Clément, J. K. Papp, M. Balasubramanian, Y. Tian, T. Lei, T. Shi, B. D. McCloskey, J. Lee, G. Ceder, Improved Cycling Performance of Li-Excess Cation-Disordered Cathode Materials upon Fluorine Substitution, *Adv. Energy Mater.* 9, 2019, 1802959.

16. R. A. House, L. Jin, U. Maitra, K. Tsuruta, J. W. Somerville, D. P. Förstermann, F. Massel, L. Duda, M. R. Roberts, P. G. Bruce, Lithium Manganese Oxyfluoride as a New Cathode Materials Exhibiting Oxygen Redox, *Energy Environ. Sci.* 11, 2018, 926–932.

17. R. Chen, S. Ren, M. Knapp, D. Wang, R. Witter, M. Fichtner, H. Hahn, Disordered Lithium-Rich Oxyfluoride as a Stable Host for Enhanced Li[+] Intercalation Storage, *Adv. Energy Mater.* 5, 2015, 1401814.

18. R. Chen, S. Ren, M. Yavuz, A. A. Guda, V. Shapovalov, R. Witter, M. Fichtner, H. Hahn, Li^{+} Intercalation in Isostructural $Li_2VO_3$ and $Li_2VO_2F$ with $O^{2-}$ and mixed $O^{2-}/F^-$ anions, *Phys.Chem.Chem.Phys.* 17, 2015, 17288–17295.

19. R. Chen, S. Ren, X. Mu, E. Maawad, S. Zander, R. Hempelmann, H. Hahn, High-Performance Low-Temperature Li[+] Intercalation in Disordered Rock-Salt Li–Cr–V Oxyfluorides, *ChemElectroChem* 3, 2016, 892–895.

20. N. Takeda, S. Hoshino, L. Xie, S. Chen, I. Ikeuchi, R. Natsui, K. Nakura, N. Yabuuch, Reversible Li Storage for Nanosize Cation/Anion-Disordered Rocksalt-Type Oxyfluorides: $LiMoO_2 - x$ LiF ($0 \leq x \leq 2$) Binary System, *J. Power Sources* 367, 2017, 122–129.

21. N. Takeda, I. Ikeuchi, R. Natsui, K. Nakura; N. Yabuuch, Improved Electrode Performance of Lithium-Excess Molybdenum Oxyfluoride: Titanium Substitution with Concentrated Electrolyte, *ACS Appl. Energy Mater.* 2, 2019, 1629–1633.

22. M. Sathiya, G. Rousse, K. Ramesha, C. P. Laisa, H. Vezin, M. T. Sougrati, M-L. Doublet, D. Foix, D. Gonbeau, W. Walker, A. S. Prakash, M. Ben Hassine, L. Dupont, J. M. Tarascon, Reversible Anionic Redox Chemistry in High-Capacity Layered-Oxide Electrodes *Nature Mater.* 12, 2013, 827–835.

23. N. Yabuuchi, M. Nakayama, M. Takeuchi, S. Komaba, Y. Hashimoto, T. Mukai, H. Shiiba, K. Sato, Y. Kobayashi, A. Nakao, M. Yonemura, K. Yamanaka, K. Mitsuhara, T, Ohta, Origin of Stabilization and Destabilization in Solid-State Redox Reaction of Oxide Ions for Lithium-Ion Batteries, *Nat. Comm.* 7, 2016, 13814.

24. D.-H. Seo, J. Lee, A. Urban, R. Malik, S. Y. Kang, G. Ceder, The Structural and Chemical Origin of the Oxygen Redox Activity in Layered and Cation-Disordered Li-Excess Cathode Materials, *Nat. Chem.* 8, 2016, 692–697.

25. E. Zhao, Q. Li, F. Meng, J. Liu, J. Wang, L. He, Z. Jiang, Q. Zhang, X. Yu, L. Gu, W. Yang, H. Li, F. Wang, X. Huang, Stabilizing the Oxygen Lattice and Reversible Oxygen Redox Chemistry through Structural Dimensionality in Lithium-Rich Cathode Oxides, *Angew. Chem. Int. Ed.* 58, 2019, 4323–4327.

26. D. Chen, W. H. Kan, G. Chen, Understanding Performance Degradation in Cation-Disordered Rock-Salt Oxide Cathodes. *Adv. Energy Mater.* 9, 2019, 1901255.

27. J. Lee, D.-H. Seo, M. Balasubramanian, N. Twu, X. Li, G. Ceder, A New Class of High Capacity Cation-Disordered Oxides for Rechargeable Lithium Batteries: Li–Ni–Ti–Mo Oxides, *Energy Environ. Sci.* 8, 2015, 3255–3265.

28. W. D. Richards, S. T. Dacek, D. A. Kitchaev, G. Ceder, Fluorination of Lithium-Excess Transition Metal Oxide Cathode Materials, *Adv. Energy Mater.* 8, 2018, 1701533.

29. M. A. Jones, P. J. Reeves, I. D. Seymour, M. J. Cliffe, S. E. Dutton, C. P. Grey, Short-Range Ordering in a Battery Electrode, the 'Cation-Disordered' Rocksalt $Li_{1.25}Nb_{0.25}Mn_{0.5}O_2$, *Chem. Commun.* 55, 2019, 9027−9030.

30. W. H. Kan, D. Chen, J. K. Papp, A. K. Shukla, A. Huq, C. M. Brown, B. D. McCloskey, G. Chen, Unravelling Solid-State Redox Chemistry in $Li_{1.3}Nb_{0.3}Mn_{0.4}O_2$ Single-Crystal Cathode Material, *Chem. Mater.* 30, 2018, 1655−1666.

31. D. Hirai, O. Sawai, T. Nunoura, Z. Hiroia, Facile Synthetic Route to Transition Metal Oxyfluorides via Reactions between Metal Oxides and PTFE, *J. Fluorine Chemistry* 209, 2018, 43–48.

32. A. Urban, A. Abdellahi, S. Dacek, N. Artrith, G. Ceder, Electronic-Structure Origin of Cation Disorder in Transition-Metal Oxides, *Phys. Rev. Lett.* 119, 2017, 176402.

33. J. Zhang, J. Huang, Y. Li, Q. Liu, Z. Yu, J. Wu, Z. Gao, S. Wu, J. Kui, J. Song, Sintering Reaction and Pyrolysis Process Analysis of Al/Ta/PTFE, *Polymers* 11, 2019, 1469–1477.

34. W.-S. Yoon, M. Balasubramanian, K. Y. Chung, X.-Q. Yang, J. McBreen, C. P. Grey, D. A. Fischer, Investigation of the Charge Compensation Mechanism on the Electrochemically Li-Ion Deintercalated $Li_{1-x}Co_{1/3}Ni_{1/3}Mn_{1/3}O_2$ Electrode System by Combination of Soft and Hard X-ray Absorption Spectroscopy, *J. Am. Chem. Soc.* 9, 2005, 17479–17487.

35. F. Lin, D. Nordlund, I. M. Markus, T.-C. Weng, H. L. Xin, M. M. Doeff, Profiling the Nanoscale Gradient in Stoichiometric Layered Cathode Particles for Lithium-Ion Batteries, *Energy Environ. Sci.* 7, 2014, 3077–3085.

36. R. Qiao, T. Chin, S. J. Harris, S. Yan, W. Yang, Spectroscopic Fingerprints of Valence and Spin States in Manganese Oxides and Fluorides, *Current Applied Physics* 13, 2013, 544–548.

37. E. Hu, X. Yu, R. Lin, X. Bi, J. Lu, S. Bak, K.-W. Nam, H. L. Xin, C. Jaye, D. A. Fischer, K. Amine, X.-Q. Yang, Evolution of Redox Couples in Li- and Mn-Rich Cathode Materials and Mitigation of Voltage Fade by Reducing Oxygen Release, *Nature Energy* 3, 2018, 690–698.

38. M. Oishi, K. Yamanaka, I. Watanabe, K. Shimoda, T. Matsunaga, H. Arai, Y. Ukyo, Y. Uchimoto, Z. Ogumi, T. Ohta, Direct Observation of Reversible Oxygen Anion Redox Reaction in Li-Rich Manganese Oxide, $Li_2MnO_3$, Studied by Soft X-ray Absorption Spectroscopy, *J. Mater. Chem. A* 4, 2016, 9293–9302.

39. C. P. Schwartz, F. Ponce, S. Friedrich, S. P. Cramer, J. Vinson, D. Prendergast, Temperature and radiation effects at the fluorine K-edge in LiF, *J. of Electron Spectrosc* 218, 2017, 30–34.

40. R. Qiao, I. T. Lucas, A. Karim, J. Syzdek, X. Liu, W. Chen, K. Persson, R. Kostecki, W. Yang, Distinct Solid-Electrolyte-Interphases on Sn (100) and (001) Electrodes Studied by Soft X-Ray Spectroscopy, *Adv. Mater. Interfaces* 1, 2014, 1300115.

41. D. Chen, J. Wu, J. K. Papp, B. D. McCloskey, W. Yang, G. Chen, Role of Redox-Inactive Transition-Metals in the Behavior of Cation-Disordered Rocksalt Cathodes, *Small* 2020, 2000656.

42. Y. Yue, N. Li, L. Li, E. E. Foley, Y. Fu, V. S. Battaglia, R. J. Clément, C. Wang, W. Tong, Redox Behaviors in a Li-Excess Cation-Disordered Mn−Nb−O−F Rocksalt Cathode, *Chem. Mater. 32,* 2020, 4490−4498.

43. Y. Matsumura, S. Wang, and J. Mondori, Mechanism Leading to Irreversible Capacity Loss in Li Ion Rechargeable Batteries, *J. Electrochem. Soc.* 142, 1995, 2914–2918.

44. C. Zhan, T. Wu, J. Lu, K, Amine, Dissolution, Migration, and Deposition of Transition Metal Ions in Li-Ion Batteries Exemplified by Mn-Based Cathodes – A Critical Review, *Energy Environ. Sci.* 11, 2018, 243–257.

45. Q. Jacquet, A. Iadecola, M. Saubanère, H. Li, E. J. Berg, G. Rousse, J. Cabana, M.-L. Doublet, J.-M. Tarascon, Charge Transfer Band Gap as an Indicator of Hysteresis in Li-Disordered Rock Salt Cathodes for Li-Ion Batteries, *J. Am. Chem. Soc.* 141, 2019, 11452−11464.

46. Y. Wang, Y. Wang, E. Hosono, K. Wang, H. Zhou, The Design of a LiFePO4/Carbon Nanocomposite with a Core-Shell Structure and its Synthesis by an In Situ Polymerization Restriction Method, *Angew. Chem. Int. Ed.* 47, 2008, 7461–7465.

47. N. Ravet, M. Gauthier, K. Zaghib, J.B. Goodenough, A. Mauger, F. Gendron, C.M. Julien, Mechanism of the Fe3+ Reduction at Low Temperature for LiFePO4 Synthesis from a Polymeric Additive, *Chem. Mater.* 19, 2007, 2595–2602.

48. J. Wang, X. Sun, Understanding and Recent Development of Carbon Coating on LiFePO4 Cathode Materials for Lithium-Ion Batteries, *Energy Environ. Sci.* 5, 2012, 5163–5185.

Table 1. Comparison of the 1st and 2nd cycle performance of the DRX cathodes.

| Samples | Theoretical capacity (mAh/g) | | Experimental values | | | | | |
| --- | --- | --- | --- | --- | --- | --- | --- | --- |
| | $Mn^{3+}/Mn^{4+}$ | Total Li content | 1st CC | 1st DC | 1st CE | 2nd CC | 2nd DC | 2nd CE |
| F0 ($Li_{1.2}Mn_{0.6}Nb_{0.2}O_2$) | 175 | 350 | 310.9 | 269.0 | 86.5 | 276.0 | 251.2 | 91.0 |
| F2.5 ($Li_{1.2}Mn_{0.625}Nb_{0.175}O_{1.95}F_{0.05}$) | 184 | 353 | 314.4 | 269.9 | 85.9 | 273.2 | 258.3 | 94.6 |
| F5 ($Li_{1.2}Mn_{0.65}Nb_{0.15}O_{1.9}F_{0.1}$) | 193 | 356 | 292.8 | 241.1 | 82.4 | 243.8 | 235.4 | 96.6 |
| F10 ($Li_{1.2}Mn_{0.7}Nb_{0.1}O_{1.8}F_{0.2}$) | 212 | 363 | 270.3 | 206.8 | 76.5 | 223.4 | 212.2 | 95.0 |

CC: Charge Capacity (mAh/g)　DC: Discharge Capacity (mAh/g)　CE: Coulombic Efficiency (%)
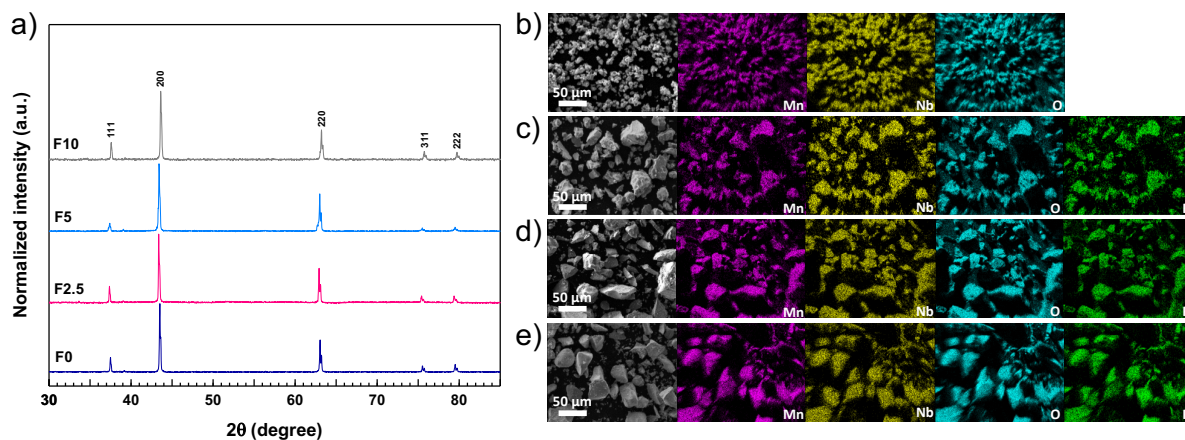
**Figure 1**. (a) X-ray diffraction patterns of the non-fluorinated (F0) and the fluorinated (F2.5, F5, and F10) as-prepared DRX powder samples, (b–e) morphological observation from SEM images and EDX elemental distribution mapping for Mn (magenta), Nb (yellow), O (cyan) and F (green): (b) F0, (c) F2.5, (d) F5 and (e) F10.
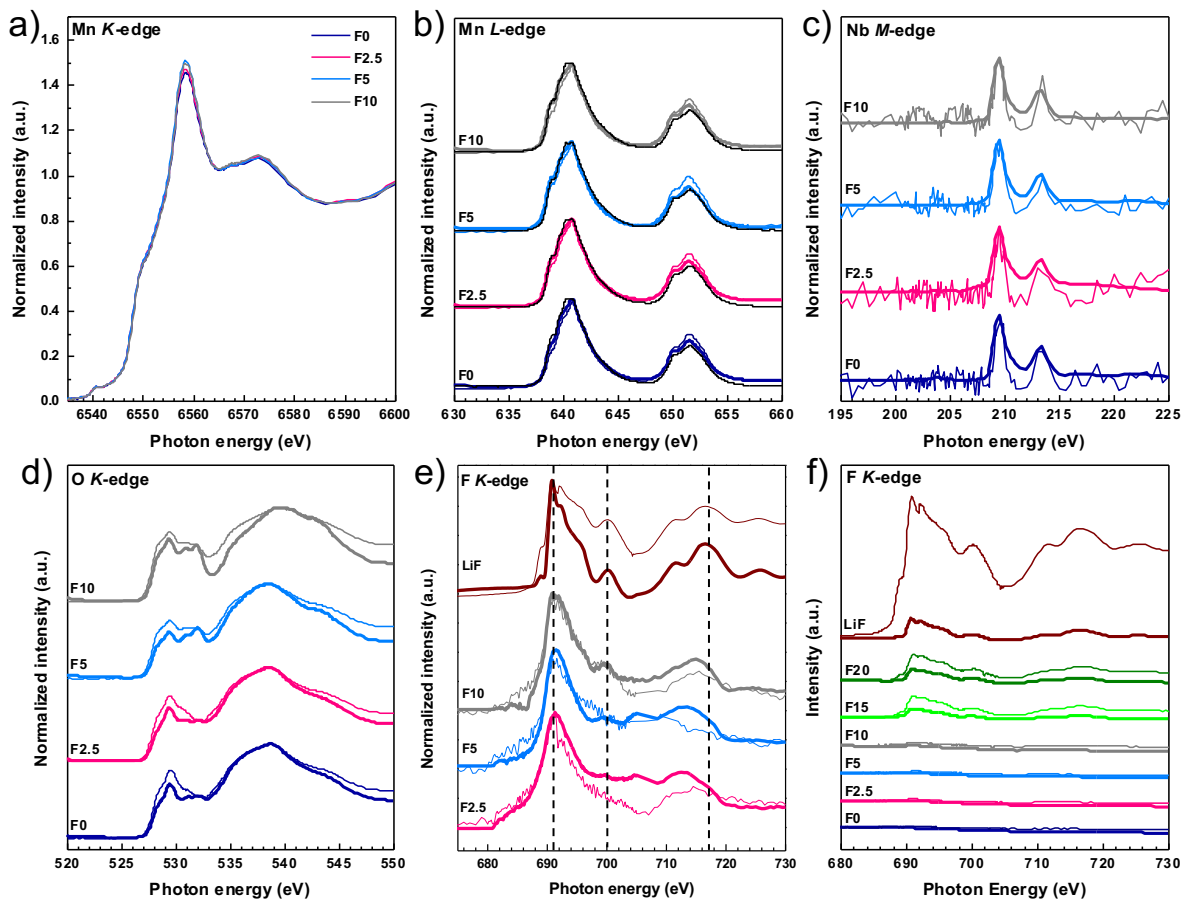
**Figure 2**. Hard and soft XAS profiles of F0, F2.5, F5 and F10: (a) Mn *K*-edge XANES spectra and normalized soft XAS spectra of: (b) Mn $L_2$- and $L_3$-edges, (c) Nb $M_4$- and $M_5$-edges, (d) O *K*-edge, (e) F *K*-edge and (f) F *K*-edge including all synthesized DRX materials. TEY spectra are shown in thick lines while FY spectra are shown in thin lines.
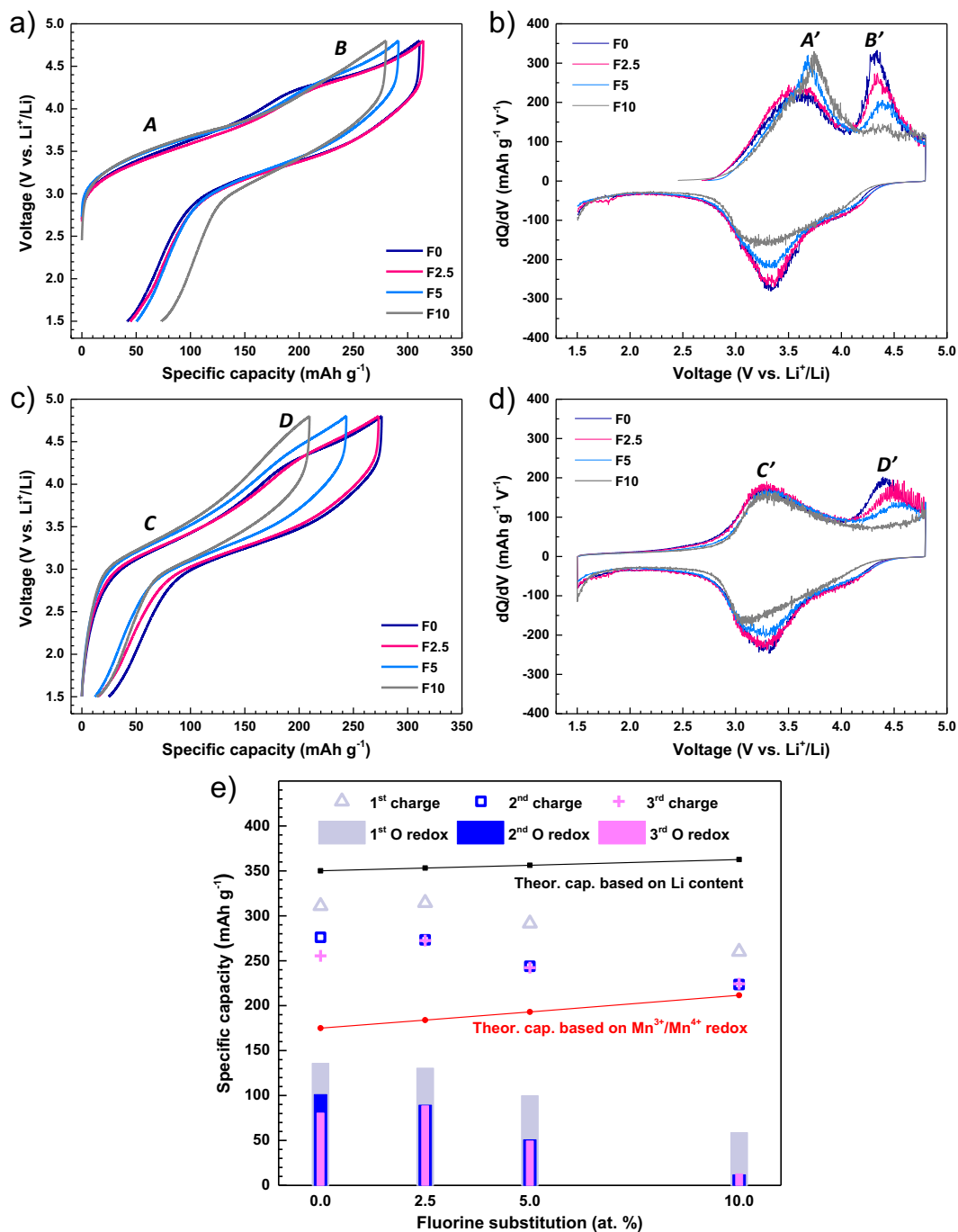
**Figure 3**. Electrochemical performance collected on F0, F2.5, F5 and F10 half-cells: voltage profiles (a, c) and the corresponding differential capacity *vs.* voltage plots (b, d) during the first cycle (a, b) and the second cycle (c, d), (e) capacity origin as a function of F content in the first cycle (grey triangle angle and bar), second cycle (blue square and bar) and the third cycle (magenta cross and bar).
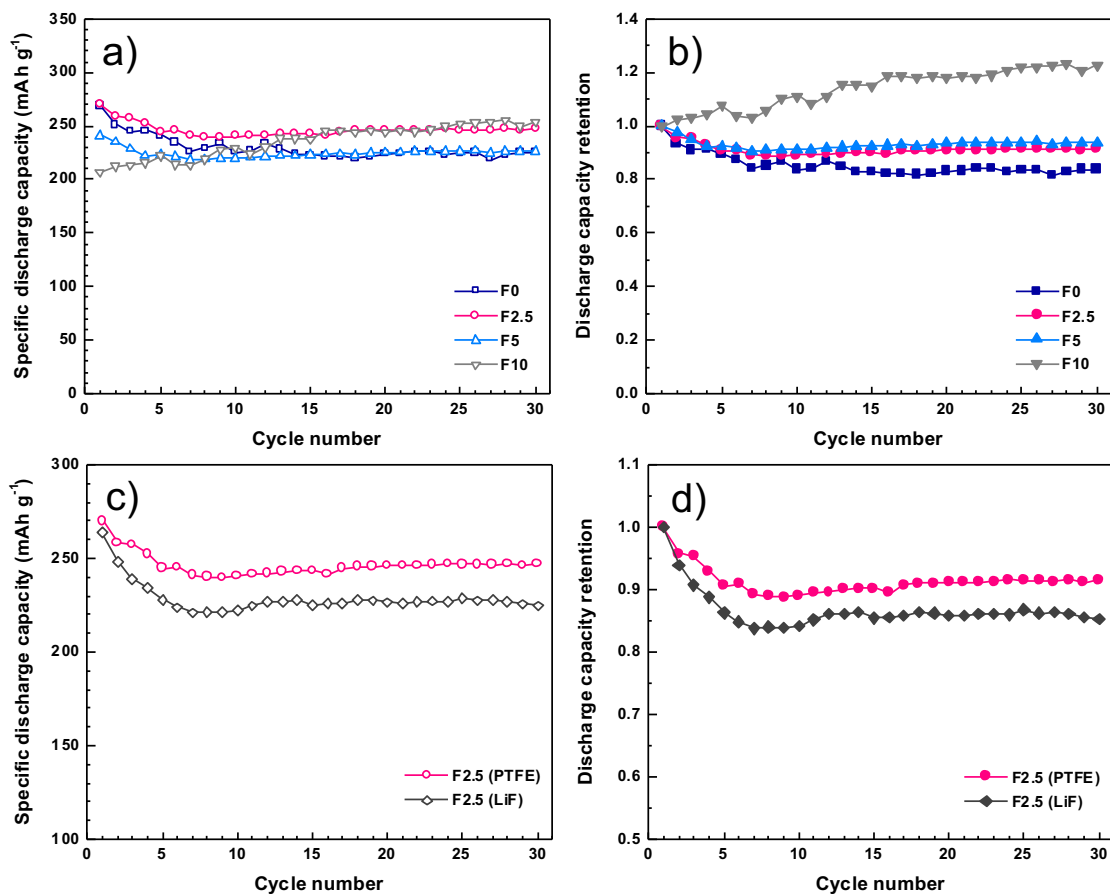
**Figure 4**. (a, b) Comparison of specific discharge capacity and capacity retention of F0, F2.5, F5 and F10 cathodes during the first 30 cycles and (c, d) comparison of specific discharge capacity and capacity retention of F2.5 prepared with PTFE (pink) and LiF (black) precursors in the first 30 cycles.
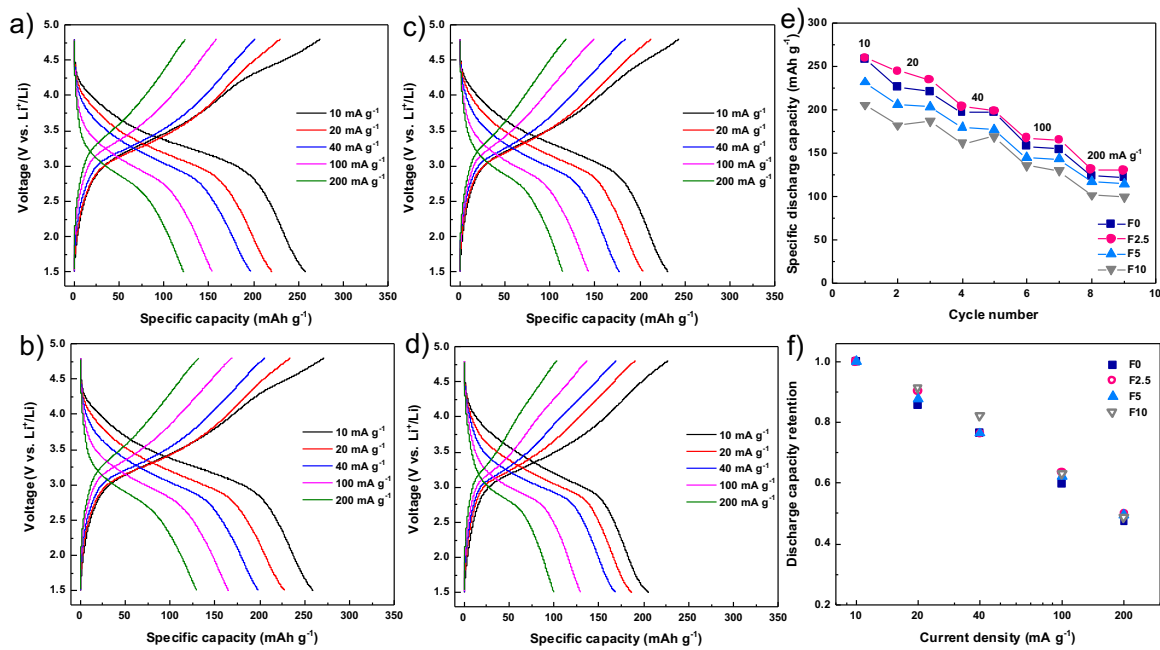
**Figure 5**. Voltage profiles of cathodes at varying current densities: (a) F0, (b) F2.5, (c) F5 and (d) F10, (e) rate capability comparison of the cathodes and (f) comparison of the discharge capacity retention as a function of current density.